

# Quantifying local heterogeneities in the 3D morphology of X-PVMPT battery electrodes based on FIB-SEM measurements

Lukas Dodell <sup>a,1</sup>, Matthias Neumann<sup>b,1,2</sup>, Markus Osenberg<sup>c</sup>, André Hilger<sup>c</sup>, Gauthier Studer<sup>d</sup>, Birgit Esser<sup>d</sup>, Ingo Manke<sup>c</sup>, Volker Schmidt<sup>a</sup>

<sup>a</sup>*Institute of Stochastics, Ulm University, 89069 Ulm, Germany*

<sup>b</sup>*Institute of Statistics, Graz University of Technology, 8010 Graz, Austria*

<sup>c</sup>*Institute of Applied Materials, Helmholtz Center for Materials and Energy, 14109 Berlin, Germany*

<sup>d</sup>*Institute of Organic Chemistry II and Advanced Materials, Ulm University, 89069 Ulm, Germany*

---

## Abstract

Organic electrode-active materials (OAMs) not only enable a variety of charge and storage mechanisms, but are also safer for the environment and of lower cost compared to materials in commonly used lithium-ion batteries. Cross-linked Poly(3)-vinyl-*N*-methylphenothiazine (X-PVMPT) is a p-type OAM which shows high performance and enables fast and reversible energy storage in different battery configurations. The performance of an OAM does not only depend on its molecular or polymer structure, but also on the structure of the composite electrode. The porous nanostructure of an electrode composed of X-PVMPT, a conductive carbon additive and binder is investigated by statistical image analysis, based on 3D image data obtained by focused-ion beam scanning-electron microscopy (FIB-SEM) measurements. Univariate probability distributions of relevant morphological descriptors as well as bivariate distributions of pairs of such descriptors are parametrically modelled, among others, by utilization of copulas in the latter case. These models are then used for quantifying local heterogeneities of X-PVMPT considered in this paper. Furthermore, it is shown that the nanostructure changes when traversing from bottom to top face of the electrode, which influences its performance. While the observed short transportation paths through the solid phase are beneficial in terms of electrical conductivity, the pathways through the pore phase influencing the effective ionic diffusivity are—in comparison—rather long.

**Keywords:** Cross-linked poly(3)-vinyl-*N*-methylphenothiazine, FIB-SEM tomography, nanostructure, parametric copula, polymer-based battery, statistical image analysis

---

<sup>1</sup>LD and MN contributed equally to this paper.

<sup>2</sup>Corresponding author. Email: neumann@tugraz.at. Phone: +43 316 873 - 4543

---

## 1. Introduction

Electrochemical energy storage is of increasing relevance in today’s technology-driven world with an ever-rising global demand for batteries. This includes electromobility and consumer electronics, but also stationary grid-storage, where low-cost and safer alternatives to the lithium-ion battery might be future technologies. Organic electrode-active materials (OAMs) are attractive candidates for alternative battery concepts, made from more abundant elements [1], being potentially cheaper and safer, and enabling a variety of charge (and concurrent ion) storage mechanisms [2, 3, 4]. Functioning under uptake of electrolyte (metal) cations (for n-type OAMs) or anions (p-type OAMs), OAMs can be used as a replacement for metal oxides in classical metal-ion batteries [5], but also function well with multivalent metal ions [6, 7, 8] as well as in anionic cell configurations [9]. Poly(3-vinyl-*N*-methylphenothiazine) (PVMPT) or its cross-linked form X-PVMPT are high-performance p-type OAMs that enable fast and reversible energy storage (under anion insertion) in batteries at high potential of 3.5 V vs Li/Li+ [10]. The charge storage mechanism [11, 12], effect of electrolyte type [13] and conductive carbon additive were studied in detail for PVMPT [14]. Due to its diminished solubility in liquid battery electrolytes [15], cross-linked X-PVMPT is a particularly relevant OAM for full cells and showed exceptional performance in Al-based batteries [16], surpassing graphite in specific capacity with high rate performance, as well as in an all-organic anion-rocking chair battery [17]. Structural engineering by changing the polymer backbone [18] effects solubility [19] and charge storage mechanism as well as rate capability [19, 20], processing abilities [21] and applicability [22, 23, 24] of phenothiazine-based redox polymers [25].

Decisive for the performance of an OAM is not only its molecular or polymer structure, but to a large extent the morphology of the composite electrode used in the battery. The composite electrode consists of the OAM as well as a conductive carbon additive and binder. Its morphology strongly influences electron- as well as ion transport, effecting the charge-storage performance. We herein investigate an X-PVMPT-based composite electrode with respect to the 3D morphology of its nanopores. For this purpose, 3D imaging is combined with methods from spatial statistics, mathematical morphology and machine learning in order to quantify the nanostructure of the considered X-PVMPT-based composite electrode. This allows us to locally evaluate porosity or

surface area per unit volume as well as to determine morphological descriptors, which are not accessible experimentally. For polymer-based battery electrodes, this approach has been used to elucidate morphological differences between PTMA, i.e. poly(2,2,6,6-tetramethyl-4-piperinidyl-*N*-oxyl methacrylate)-based, electrodes manufactured either with polyvinylidenefluoride (PVDF) or with water-soluble binder [26]. Recently, this methodology also revealed the impact of cross-linking in PTMA-CMK8 electrodes on their morphology [27]. In both studies, the morphology on the micrometre-scale was quantified based on 3D-image data acquired by synchrotron-tomography [28, 29].

In the present paper, we consider the 3D morphology of an X-PVMPT electrode on the nanometer-scale. Thus, focused-ion beam scanning-electron microscopy (FIB-SEM) [30, 31] is used for image acquisition which allows for a voxel resolution of 10 nm. As in [27], image segmentation, i.e. the detection of pore voxels based on greyscale images, is performed by machine learning using the software ilastik [32]. The focus of the subsequent statistical image analysis is on the quantification of local heterogeneities. Going beyond the descriptive analysis performed in [26, 27], we use parametric statistics to model both the univariate distribution of local morphological descriptors as well as bivariate distributions of pairs of such descriptors. Doing so, the heterogeneity of the complex nanoporous morphology is characterized by a small number of model parameters. Moreover, by parametric modeling of the bivariate distributions, we obtain analytical formulas for the corresponding conditional distributions, such as, e.g., the distribution of the local surface area per unit volume conditioned on a predefined value of local porosity. From the conditional distributions, in turn, one can easily derive the corresponding expectations, variances or quantiles, which elucidate quantitative relationships between pairs of local morphological descriptors. For this modeling approach we build upon methodologies previously developed for quantifying the 3D morphology of paper-based materials [33, 34]. Furthermore, structural gradients within the X-PVMPT-based composite electrode considered in the present paper are revealed.

## 2. Materials and 3D Imaging

### 2.1. Description of electrode material

The crosslinked X-PVMPT polymer with 10 mol% of the crosslinker was synthesized using the same procedure as reported in [15, 16]. Composite electrodes were prepared using 50 wt.% X-PVMPT,

45 wt.% carbon additive (Super C65, Timcal) and 5 wt.% PVdF (Kynar HSV 900, Arkema). X-PVMPT and carbon black were pre-dried in a vacuum oven ( $10^{-3}$  mbar) at 60 °C for 24 h, then pre-mixed using a planetary centrifugal mixer (1500 rpm, 15 min, ARM 310, Thinky mixer). The binder was added as a 5 wt.% PVDF in *N*-methyl-2-pyrrolidone (NMP, Acroseals, Thermo scientific, 99.5%, stored over molecular sieves) solution, and the composite mixed. Finally, stepwise NMP additions and mixing steps (1500 rpm, 15 min) were performed until a honey-like viscosity was obtained. The resulting paste was blade-coated onto KOH-etched aluminum foil (1235 aluminum foil, H18 hard state, 20  $\mu\text{m}$  from Gelon LIB), with a wet-film thickness of 100  $\mu\text{m}$ . The coated foil was dried at ambient pressure at 60 °C for 24 h, and electrodes with a diameter of 12 mm were punched out with an electrode-punching device (EL-Cut from EL-CELL). The active material (X-PVMPT) mass loadings of the electrodes lay between 0.22 mg/cm<sup>-2</sup> and 0.24 mg/cm<sup>-2</sup>. Note that the theoretical specific capacity of X-PVMPT for a one-electron process is 112 mAh/g, while the practical capacity lies close to this value in Li-half cells [15].

## 2.2. 3D imaging by FIB-SEM tomography

For 3D tomography using FIB-SEM, the polymer sample was first mounted on a standard 12.5 mm aluminium SEM stub. For this purpose, a 1 mm  $\times$  3 mm piece was cut out with a scalpel and glued to the SEM holder with the aluminum conductor side using a carbon adhesive pad. A copper tape was glued over one side of the sample to ensure good conductivity of the sample during SEM imaging. The sample was then inserted into the ZEISS Crossbeam 340 of the Corelab Correlative Microscopy and Spectroscopy (CCMS) at Helmholtz-Zentrum Berlin (HZB). Using a gallium ion beam current of 15 nA (at 30 keV), the polymer material and parts of the underlying aluminum conductor were first removed in a 30  $\mu\text{m}$   $\times$  30  $\mu\text{m}$  area in the centre of the polymer sample. The cross-section exposed for imaging was polished with an ion current of 300 pA. A low acceleration voltage of 1 keV was used for imaging to minimize the depth of electron penetration into the sample. An image size of 2048 pixels  $\times$  1536 pixels was selected for imaging with an acquisition time of 20.5 seconds per image. A chamber mounted SE2 detector was used for serial imaging. With a field of view of 20.5  $\mu\text{m}$ , this resulted in a pixel size of 10 nm. The ion beam was then used to remove a 10 nm layer of the sample between each image using the 300 pA current at 30 keV, resulting in a 3D data set with an isotropic voxel edge length of 10 nm.

### 3. Pre-processing and segmentation of image data

Using the results of the FIB-SEM measurements described in Section 2.2, the porous nanostructure of the X-PVMPT-based electrode material was reconstructed from 3D-greyscale image data by a phase-based segmentation. Prior to the segmentation, pre-processing of the greyscale image data was required. First, a drift correction was applied. This was done by registering the areas above the current cross-section. These areas had not yet been cut by the gallium beam and therefore contained image information about the surface of the unaltered sample. Therefore, features detected in these areas had to be constantly moving towards the cutting edge of the forward moving cross-section. Any non-constant motion was corrected using the scale-invariant feature transform (SIFT) algorithm [35], implemented in FIJI [36]. Note that this correction has been applied to the greyscale image data. Subsequently, the sample is aligned to the coordinate system of the sampling window, as shown in Figure 1. The  $x$ -axis goes from left to right, the  $z$ -axis from bottom to top, and the  $y$ -axis goes through the image slices starting at the first image slice.

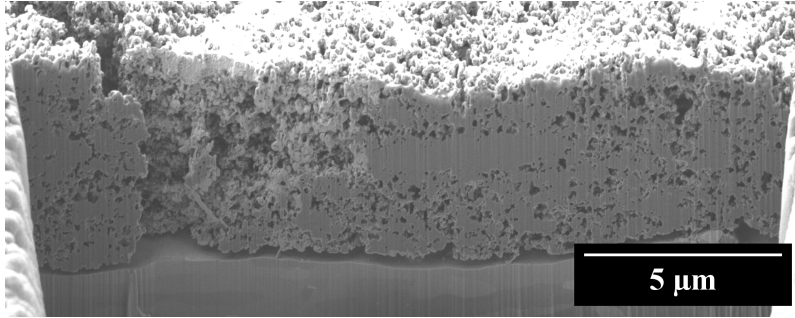


Figure 1: 2D Slice of greyscale image data obtained by FIB SEM tomography.

In the next step, to analyze the nanostructure of the electrode, a phase-based segmentation of the underlying greyscale image data obtained by FIB-SEM tomography was performed. This means that each voxel of the image is assigned to either solid, pores or background. Note, however, that the electrode material depicted in the image data has a large diagonal crack, see Figure 1. This is not only problematic in terms of segmentation, but also for the subsequent statistical analysis of the segmented nanostructure. Therefore, only a cutout, visualized in Figure 2a, was used for statistical image analysis. To segment the cutout into solid phase and the union of pores and background, a random forest classifier [37] was trained using the software ilastik [32]. The training

was performed based on hand-labeled data. Two hand-labeled slices are shown in Figures 2c and 2d, where in the latter case a 2D slice is depicted which is orthogonal to that shown in Figure 2c. The trained random forest allows us to decide for each voxel whether it belongs to the solid phase. Details are provided in the supplementary information. Finally, to distinguish between background and pores in the complement of the solid phase, a so-called rolling ball algorithm [38] with a radius of 20 voxels ( $0.2\ \mu\text{m}$ ) has been used, which was previously applied for PTMA-based battery electrodes [26, 27]. A 2D slice of the final segmentation is shown in Figure 2b.

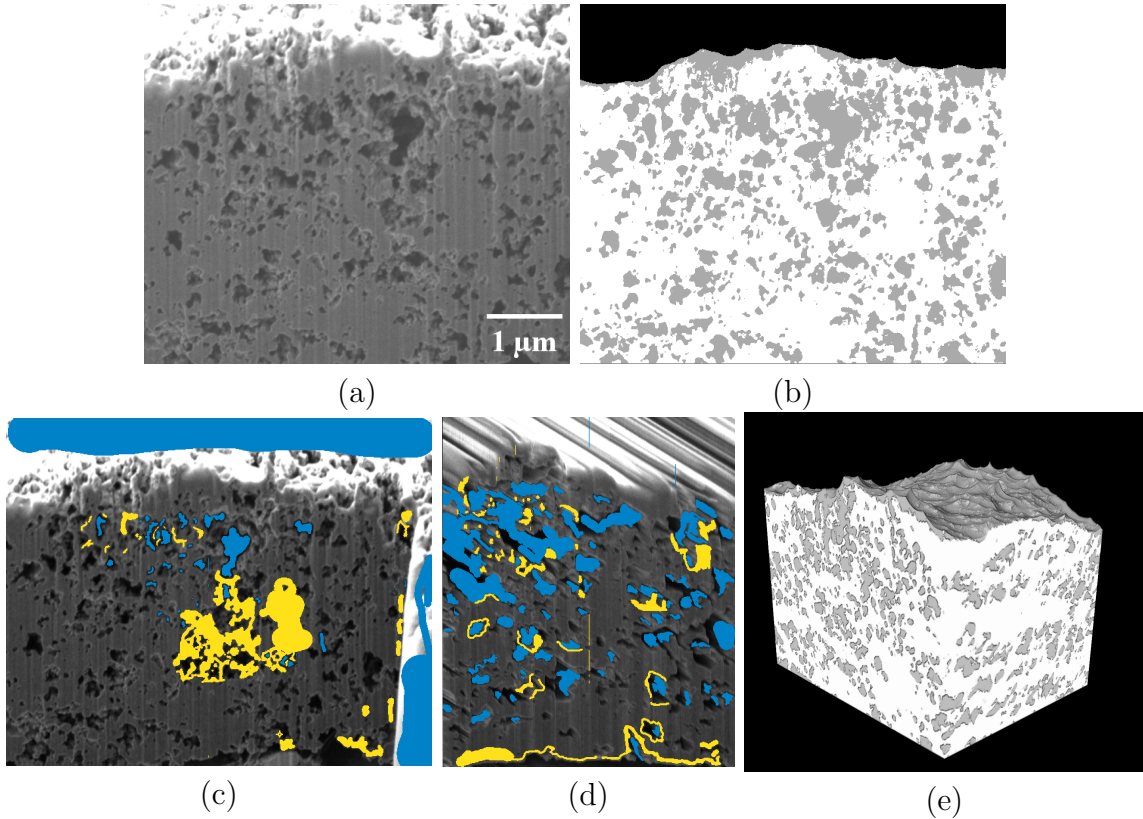


Figure 2: Cutout of FIB-SEM image data (a), corresponding 2D slice of segmentation into solid-phase (white), pores (grey) and background (black) (b), hand-labeling of image data: blue color represents background and pores, whereas yellow represents the solid phase (c,d), 3D rendering of the segmented image data (e)

## 4. Statistical analysis and modeling of segmented image data

### 4.1. Morphological descriptors

Using tools of statistical image analysis, the segmentation of image data into solid and pore phases allows for a quantitative characterization of electrode nanostructures and, in particular, local heterogeneities thereof. For this purpose, morphological descriptors of the nanostructure are globally and locally evaluated. The morphological descriptors considered in the present paper are the thickness  $\delta$ , the porosity  $\varepsilon$ , the surface area between solid and pore phases per unit volume  $S$  as well as the mean geodesic tortuosity of solid- and pore-phase, denoted by  $\tau_s$  and  $\tau_p$ , respectively. These descriptors are crucial for battery electrodes, since thickness influences the capacity of the electrode, electrochemical reactions take place at the surface area, while porosity and mean geodesic tortuosities strongly influence effective transport properties such as effective ionic diffusivity and effective electric conductivity. Quantitative relationships of the latter are discussed in Chapter 5 of [39].

Global morphological descriptors are computed based on the complete image as sampling window. For the computation of local descriptors we consider non-overlapping square-shaped cutouts with side length of 1  $\mu\text{m}$ , the centers of which are arranged on a regular hexahedral grid, in the plane parallel to the aluminum foil. For each of these cutouts the above mentioned morphological descriptors are determined, where the full thickness is taken into account. Doing so, we follow the previously used approach for investigating local heterogeneities in polymer-based batteries [26, 27] and paper-based materials [33, 34]. Then, we get empirical distributions of local morphological descriptors, which are parametrically modeled as stated in Section 4.2 below.

For a given sampling window, the thickness of the electrode  $\delta$  is computed as follows. For each line of voxels, which is orthogonal to the aluminum foil, the corresponding thickness is defined as the maximum distance between two voxels on this line belonging to the solid phase of the electrode. The average of these distances over all lines contained in the sampling window is considered to be the thickness of the electrode in this sampling window. The porosity  $\varepsilon$  is determined by the point-count method [40], i.e., the porosity is the ratio of pore voxels over all voxels of the electrode within the sampling window. The surface area per unit volume  $S$  is computed as the surface area between solid and pores in the considered sampling window divided by the volume



of the sampling window. For the computation of surface areas from voxelized image data, we use the algorithm proposed in [41]. Finally, we consider the mean geodesic tortuosity which is a purely geometrical descriptor quantifying the windedness of shortest transportation paths through a given phase. It is defined as the expected shortest path length from a predefined starting point at the bottom of the electrode to the top of the electrode through the phase of interest, which is normalized by the local thickness of the electrode at the starting point. Note that there are several types of tortuosity investigated in the literature [39, 42, 43]. Even if the definition of mean geodesic tortuosity considered in the present paper is a purely geometrical descriptor of electrode nanostructure, it strongly correlates with effective transport properties such as effective diffusivity, effective conductivity or permeability [44, 45]. To compute the mean geodesic tortuosity of a phase in a given sampling window, the shortest pathways through this phase are determined by applying the Dijkstra algorithm [46] on the voxel grid. When computing mean geodesic tortuosity on local cutouts as sampling windows, the starting points of the paths are located within these local cutouts, while the paths themselves are allowed to leave the sampling window in order to avoid a strong influence of edge effects.

#### *4.2. Parametric modeling of local morphological descriptors*

##### *4.2.1. Univariate probability densities of single descriptors*

For fitting parametric probability distributions to empirical distributions of the computed local descriptors, namely porosity  $\varepsilon$ , thickness  $\delta$ , surface area per unit volume  $S$  and mean geodesic tortuosity of solid-phase and pore-phase  $\tau_s$  and  $\tau_p$ , respectively, we proceed as follows. For each descriptor, we consider various families of parametric distributions as candidates. For each of these families, parameter fitting is performed by maximum likelihood estimation. Finally, we choose the distribution where the maximum likelihood is largest over all candidate families of distributions. At this, the maximum likelihood is penalized by the number of fitted parameters by means of Akaike's information criterion [47]. In this way, for the five local morphological descriptors mentioned above, we selected a Maxwell-Boltzmann distribution  $\text{MB}(\mu_M, \sigma_M)$ , Rayleigh distribution  $\text{R}(\mu_R, \sigma_R)$  and shifted Gamma distribution  $\Gamma(a_\Gamma, \sigma_\Gamma, \mu_\Gamma)$ , as well as mixtures of Gaussian and beta distributions, denoted by  $\text{N}(\mu_1, \mu_2, \sigma_1, \sigma_2, p_N)$  and  $\text{Beta}(\alpha_1, \alpha_2, \beta_1, \beta_2, p_B)$  for parameters  $\mu_M, \mu_R, \mu_\Gamma, \mu_1, \mu_2 \in \mathbb{R}, \sigma_M, \sigma_R, a_\Gamma, \sigma_\Gamma, \sigma_1, \sigma_2, \alpha_1, \alpha_2, \beta_1, \beta_2 > 0$  and  $0 \leq p_N, p_B \leq 1$ . The



probability density functions of these distributions are provided in the supplementary information. The fitted parameters are presented in Table 3 below.

#### 4.2.2. Copula-based bivariate densities of descriptor pairs

The bivariate probability densities of descriptor pairs could simply be modelled as products of the corresponding univariate densities considered in Section 4.2.1. However, this would require that the underlying local morphological descriptors would not be (or, at least be only weakly) correlated. But, this is not the case, as can be seen in Table 1.

	$\varepsilon$	$\delta$	$S$	$\tau_s$	$\tau_p$
$\varepsilon$	1.0	0.55	0.86	-0.59	0.80
$\delta$		1.0	0.58	-0.48	0.46
$S$			1.0	-0.64	0.59
$\tau_s$				1.0	-0.46
$\tau_p$					1.0

Table 1: Correlation matrix of local morphological descriptors  $\varepsilon$ ,  $\delta$ ,  $S$ ,  $\tau_s$  and  $\tau_p$ .

Moreover, in most cases, the univariate densities considered in Section 4.2.1 are not Gaussian, see Figures 4 and 5. Therefore, the bivariate probability densities of descriptor pairs are modelled by means of so-called copulas [33]. This approach is advantageous in a sense that the complexity of the model is split into modeling the univariate marginal distributions and modeling the copula, where the copula contains the information on the interdependence of the individual morphological descriptors.

For modeling the bivariate probability densities of descriptor pairs consisting of local porosity and one of the remaining four morphological descriptors, we consider one-parametric Archimedean copulas [48] as model type. It turned out that in all four cases the best fit was obtained by a Frank copula  $C : [0, 1]^2 \rightarrow [0, 1]$ , defined by

$$C(u, v) = -\frac{1}{\theta} \log \left( 1 + \frac{(e^{-\theta u} - 1)(e^{-\theta v} - 1)}{e^{-\theta} - 1} \right)$$

for any  $u, v \in [0, 1]$ , where  $\theta \in \mathbb{R} \setminus \{0\}$  is some model parameter. Plugging the parametric distribution functions and probability densities of the univariate distributions as well as the parametric

copula into the formulas for conditional probability densities, we obtain analytical formulas for the latter ones. These analytical formulas fully quantify the relationship between pairs of local morphological descriptors. In particular, they can be used to compute conditional expectations and quantiles of a morphological descriptor for fixed porosity. The latter can be used for predictions of local morphological descriptors based on local porosity.

## 5. Results and discussion

### 5.1. Results

From visual inspection of the cutout shown in Figure 2a it seems that the porosity of the sample depends on the height, i.e., the  $z$ -value of the location we look at. This is confirmed by the results of statistical image analysis, when we determine porosity and boundary length of the interface between pores and solid at a given height  $z \in [0, 4]\mu\text{m}$ , see Figure 3. Note that for this purpose, we consider the complete sample in the  $xy$ -plane. Here we can see that both characteristics strongly depend on the  $z$ -position as porosity and boundary length increase approaching the top part of the electrode.

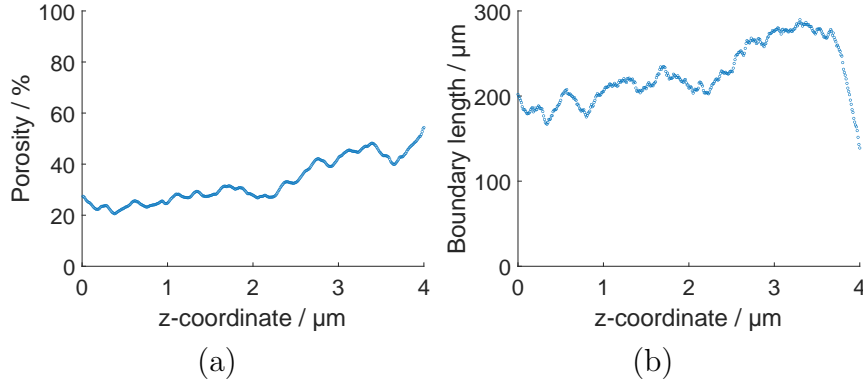


Figure 3: Porosity (a) and boundary length (b) in dependence on the height  $z$  within the electrode.

Furthermore, the spatial gradient of the boundary length presented in Figure 3 shows that the surface area per unit volume in 3D is increasing with an increasing distance to the aluminum foil. This observation is in good accordance with the spatial gradient observed for porosity as—depending on the shape of the phases—the surface area typically takes its maximum when both phases, pores and solid, have nearly the same volume fraction. For the PTMA-based electrodes considered in [26], e.g., the surface area per unit volume on the micro-scale takes its maximum

at a volume fraction of PTMA at 60%. The values of global morphological descriptors for the X-PVMPT-based composite electrode considered in the present paper, which have been obtained by averaging over results for all sampling windows, are given in Table 2.

$\varepsilon$	$\delta$	$S$	$\tau_s$	$\tau_p$
37 %	4.02 $\mu\text{m}$	8.82 $\mu\text{m}^{-1}$	1.04	1.24

Table 2: Global morphological descriptors, obtained by averaging over results for all sampling windows.

#### 5.1.1. Univariate distributions of local morphological descriptors

To investigate local heterogeneities of the X-PVMPT-based composite electrode we first computed the values of  $\varepsilon$ ,  $\delta$ ,  $S$ ,  $\tau_s$  and  $\tau_p$  for each of the non-overlapping square-shaped cutouts with side length of 1  $\mu\text{m}$ . The corresponding empirical distributions were obtained by kernel density estimation using a Gaussian kernel. The fitted parametric families of distributions and the corresponding parameter values are summarized in Table 3. Note that in the following figures the empirical distributions are referred to as “data”, the fitted parametric univariate distributions as “model”.

descriptor	distribution type	parameter values
$\varepsilon$	Beta mixture	$\alpha_1 = 109.43$ , $\alpha_2 = 125.79$ , $\beta_1 = 65.44$ , $\beta_2 = 47.74$ , $p_B = 0.59$
$\delta$	Maxwell-Boltzmann	$\mu_M = 3.46$ , $\sigma_M = 0.35$
$S$	Gaussian mixture	$\mu_1 = 13.1$ , $\mu_2 = 10.46$ , $\sigma_1 = 0.87$ , $\sigma_2 = 1.06$ , $p_N = 0.56$
$\tau_s$	Rayleigh	$\mu_R = 1.01$ , $\sigma_R = 0.024$
$\tau_p$	Gamma	$a_\Gamma = 2.97$ $\mu_\Gamma = 1.14$ , $\sigma_\Gamma = 0.037$

Table 3: Morphological descriptors, fitted parametric distribution types, and parameter values

We first consider the empirical probability density of the local thickness  $\delta$ , which is shown in Figure 4a. There is only little variability visible for  $\delta$ , being almost symmetrically distributed around the mean. As parametric model, a Maxwell-Boltzmann distribution was fitted. Looking at the results obtained for porosity  $\varepsilon$ , see Figure 4b, a bimodal density can be observed. The modes are located at 23% and 35%, where the distribution is less concentrated at the latter one. The values of  $\varepsilon$  vary from 15% up to 50%, which shows a strong heterogeneity of local porosity. Considering the porosity  $\varepsilon$  as volume fraction, it takes values between 0 and 1. Thus, having in mind that the kernel density estimate of  $\varepsilon$  is bimodal, a mixture of two Beta distributions has been chosen as a parametric model.

A further important morphological descriptor of battery electrodes is the surface area of the solid phase, because it heavily influences the electrochemical processes in the electrode. A larger surface area per unit volume, denoted by  $S$ , can be advantageous, as it corresponds to the amount of interface at which electrolyte and solid phase can interact. The shape of the density of  $S$ , visible in Figure 4c, results from the correlation between volume fraction and surface area per unit volume, also discussed in the context of the spatial gradients shown in Figure 3. The surface area per unit volume tends to take its maximum in case that the fraction of solid and pores are nearly identical. Because of this interdependence of local porosity  $\varepsilon$  and local specific surface area  $S$  and in view of the bimodality of the density of  $\varepsilon$ , a bimodal parametric model, namely a mixture of two Gaussian distributions, was chosen for  $S$ .

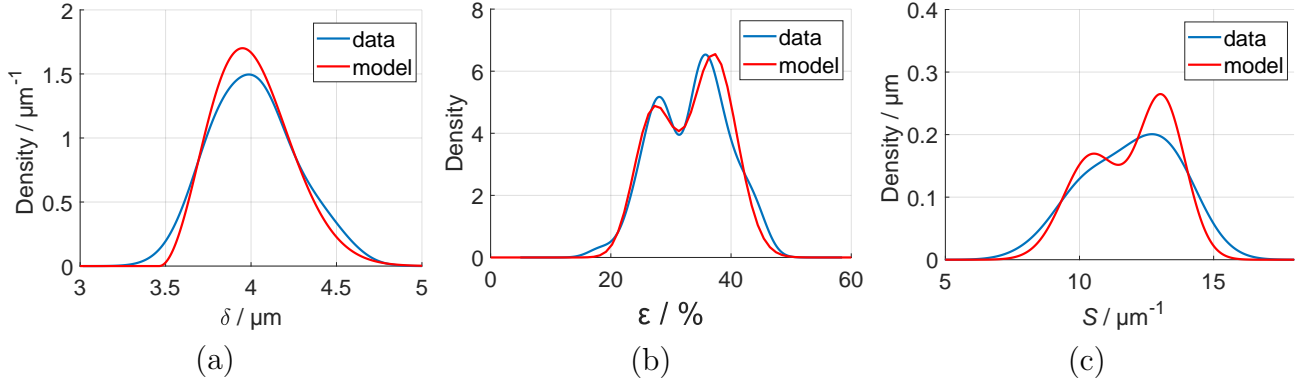


Figure 4: Empirical probability density (data) and fitted parametric density (model) of local thickness  $\delta$ , local porosity  $\varepsilon$ , and local surface area per unit volume  $S$ .

Last but not least, we look at a morphological descriptor which quantifies the lengths of shortest pathways through a given material phase, namely the so-called mean geodesic tortuosity, see Section 4.1 for details. The empirical density of the mean geodesic tortuosity  $\tau_s$  in the solid phase is shown in Figure 5a. For large parts of the electrode, straight pathways in the solid-phase with almost no obstruction from the top- to the bottom-face of the electrode can be found. This results in a distribution, which is mainly concentrated at small tortuosity values of about 1.04. Note that for PTMA-CMK8 electrodes comparably short—or even shorter—transportation pathways are observed in the solid phase at the microscale [27]. Compared to nanostructured  $\text{LiNi}_{1/3}\text{Mn}_{1/3}\text{Co}_{1/3}\text{Co}_2$  (NMC) active material particles, 1.04 is rather low. For differently manufactured nanostructured NMC particles, the mean geodesic tortuosity of solid and pores exceeds 1.04 [49]. Nevertheless,

in the present paper,  $\tau_s$  still locally reaches values up to 1.1. This could be explained by the higher porosity in certain areas, which leads to less pathways in the solid phase and, therefore, to larger values of  $\tau_s$ . Thus, a Rayleigh distribution [50] was used for the fitting of a parametric model. Moreover, the empirical density of mean geodesic tortuosity of pore phase  $\tau_p$ , depicted in Figure 5b, was analyzed. This descriptor is of even higher importance than the mean geodesic tortuosity in the solid phase  $\tau_s$ , since the supply of electrons in the solid phase is rarely a limiting factor regarding the electrochemical performance of electrodes. The values of  $\tau_p$  range from 1.15 up to 1.5 with highest concentration at about 1.22. This effect can again be explained by the local behavior of porosity, since there are in general much fewer possible pathways in the pore space, increasing the shortest path length and, therefore, increasing the mean geodesic tortuosity  $\tau_p$ . It turned out that a gamma distribution fits the empirical density of  $\tau_p$  quite well, see Figure 5b.

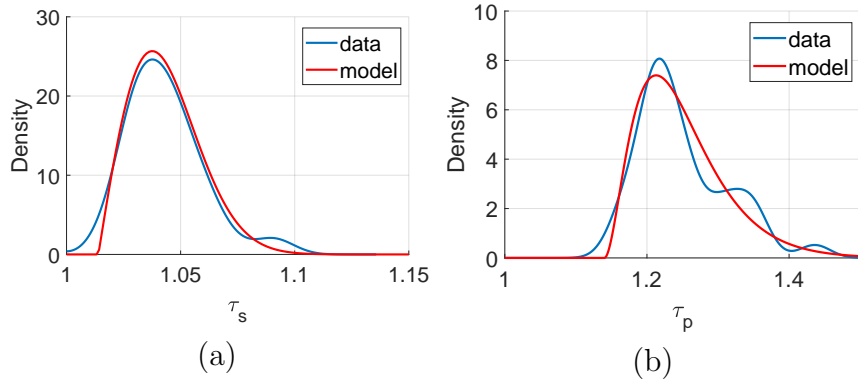


Figure 5: Empirical probability density (data) and fitted parametric density (model) of means geodesic tortuosities,  $\tau_s$  and  $\tau_p$ , in the solid (a) and pore phase (b), respectively.

### 5.1.2. Bivariate distributions of descriptor pairs

After having considered the fitting of univariate probability densities for single morphological descriptors in Section 5.1.1, we now explain which bivariate parametric densities were selected for descriptor pairs, consisting of  $\varepsilon$  and one of the remaining four descriptors  $\delta$ ,  $S$ ,  $\tau_s$  and  $\tau_p$ . In particular, using bivariate kernel density estimates we fitted one-parametric Archimedean copulas, see Table 4.

In the next step, using the copula-based representation formula for bivariate probability densities stated in Section 4.2.2, two-dimensional density plots for descriptor pairs were determined, where a nice coincidence between empirical and fitted parametric densities can be observed for all four

2nd descriptor	fitted parameter of Frank copula
$\delta$	$\theta = 4.09$
$S$	$\theta = 9.77$
$\tau_s$	$\theta = 8.89$
$\tau_p$	$\theta = -4.96$

Table 4: Fitted parameters of the Frank copula for descriptor pairs, where the first descriptor is the porosity  $\varepsilon$ .

pairs of local microstructure descriptors, see Figure 6. Note that black contour lines in the plots resemble the 75%-, 50%- and 25% - quantiles, white lines represent the conditional mean values for given porosities.

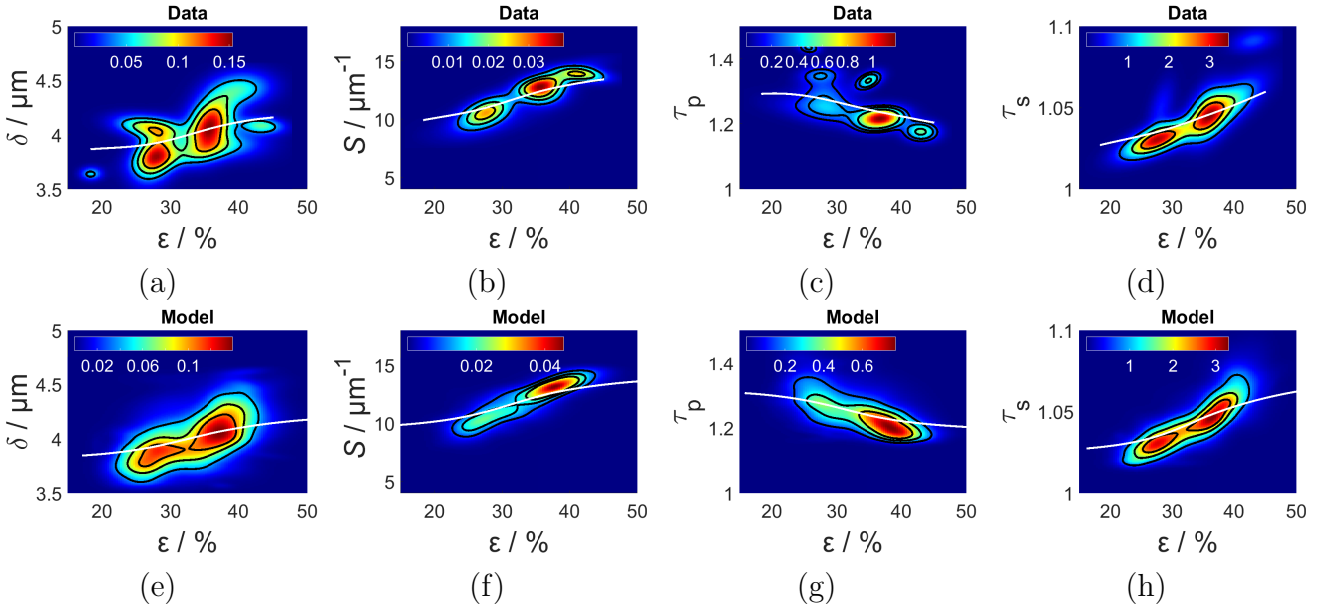


Figure 6: Bivariate empirical densities (top row) and fitted parametric densities (bottom row) of pairs of local microstructure descriptors. The bivariate probability densities are visualized as heat maps, where the white lines represent the (conditional) mean values for given local porosities. The black contour lines are the 25%-, 50%- and 75%-quantiles, respectively.

By visual inspection of the bivariate densities shown in Figure 6, it becomes evident that the local porosity  $\varepsilon$  is correlated with the remaining four descriptors  $\delta$ ,  $S$ ,  $\tau_s$  and  $\tau_p$ . Regarding the pair  $(\varepsilon, \delta)$  of thickness and porosity, considered in Figures 6a and 6e, we can see that these two descriptors are positively correlated, see also Table 1. This behaviour is sensible in a way that the electrode seems to be thicker in the center of the image data cutout, where we also observed large porous regions compared to other parts of the data, see Figure 2b.

Furthermore, looking at the bivariate density of  $(\varepsilon, S)$ , i.e. local porosity and surface area per unit volume, presented in Figures 6b and 6f, we also observe a positive correlation. On the other hand, the bivariate density of  $(\varepsilon, \tau_p)$ , i.e. porosity and mean geodesic tortuosity of the pore phase, shown in Figures 6c and 6g, indicates a negative correlation. This is not surprising, since decreasing the porosity means less pore space and, therefore, fewer pathways that can be traversed, which results in longer pathways and, consequently, increases the mean geodesic tortuosity of the pore space. With similar arguments as above, the positive correlation of  $\varepsilon$  and  $\tau_s$ , i.e. local porosity and mean geodesic tortuosity of the solid phase, can be explained. Decreasing porosity increases the volume fraction of solid phase and, thus, the number of possible pathways through the solid phase, which decreases the average length of shortest pathways in this phase.

## 5.2. Discussion

The 3D morphology of the X-PVMPT-based composite electrode investigated in this paper shows two different types of structural heterogeneity. On the one hand, we observed that the porosity of the sample is highly dependent on the  $z$ -position in the electrode, meaning that the electrode material is more porous near the top face. These porous regions at the top also have coarser surfaces, since the boundary area of the solid phase is larger at the top face of the electrode, see Figure 3. These spatial gradients might presumably arise during the drying process. In order to support this conjecture and to achieve a detailed understanding of the relationships between process parameters and the gradient of porosity, further research is required including 3D imaging of differently manufactured X-PVMPT electrodes.

On the other hand, we observed considerable local heterogeneities of the electrode material for different 3D cutouts along the  $(x, y)$ -plane. This can be seen by the high variances of the univariate distributions of the local morphological descriptors fitted in Section 5.1.1 to segmented image data. Furthermore, we observed a positive correlation between local porosity  $\varepsilon$  and thickness  $\delta$  as well as between  $\varepsilon$  and surface area per unit volume  $S$ . However, note that the values of local thickness  $\delta$  of the electrode material show relatively little variation and are pretty closely grouped around their mean value, see Figure 4a. The mean geodesic tortuosity of the solid phase  $\tau_s$  showed values close to 1, which implicates short transportation paths through the solid phase. In contrast we have seen that the mean geodesic tortuosity of the pore phase  $\tau_p$  exhibits larger values, which tells us



that the paths through the porous phase are much more winded.

## 6. Conclusion

Our analysis of the X-PVMPT-based composite electrodes provides valuable insights into the nanostructural properties and local heterogeneities of its 3D morphology. The combination of FIB-SEM tomography, which achieved a voxel resolution of 10 nm, and image-segmentation techniques allowed for a detailed morphological characterization of the electrode. The investigations performed in this study focused on key morphological descriptors such as thickness, porosity, surface area per unit volume, and mean geodesic tortuosity for both, solid and pore phases. These descriptors are crucial for the performance of the electrode. In particular, the porosity was observed to be highly variable and dependent on the  $z$ -position within the electrode, with higher porosity and coarser surfaces towards the top. This heterogeneity was further supported by the distributions of local descriptors, which were modeled using parametric probability distributions. The bivariate densities, modeled with Frank copulas, revealed quantitative relationships between descriptors, especially the correlations between porosity and the remaining four morphological descriptors. Notably, the values obtained for the local mean geodesic tortuosities  $\tau_s$  and  $\tau_p$  indicated that pathways through the solid phase were relatively straight, whereas those through the pore phase were more winded, impacting the overall charge-transport properties through these two phases. These insights emphasize the critical role of the nanostructure with respect to the performance of organic electrode-active materials (OAMs). Understanding and controlling these morphological features can pave the way for optimizing battery design for X-PVMPT electrodes and enhancing the efficiency of polymer-based batteries, as it was already done for NMC-based electrodes, see, e.g. [51]. The results obtained in the present paper provide a foundation for future research on the morphological optimization of OAM-based electrodes, contributing to the advancement of safer, more efficient, and cost-effective battery technologies.

## Acknowledgement

This research has been supported by the German Research Foundation (DFG) under grants 441292784 and 441215516, within Priority program 2248 “Polymer-based batteries” of DFG. Moreover, this research was funded by DFG under Project ID 390874152 (POLiS Cluster of Excellence,

EXC 2154). The present paper contributes to the research performed at CELEST (Center for Electrochemical Energy Storage Ulm-Karlsruhe).

## References

- [1] J. Kim, Y. Kim, G. Kwon, Y. Ko, and K. Kang. Organic batteries for a greener rechargeable world. Nature Reviews Materials, 8:54–70, 2022.
- [2] B. Esser. Redox polymers as electrode-active materials for batteries. Organic Materials, 1:063–070, 2019.
- [3] B. Esser, F. Dolhem, M. Becuwe, P. Poizot, A. Vlad, and D. Brandell. A perspective on organic electrode materials and technologies for next generation batteries. Power Sources, 482, 2021.
- [4] P. Poizot, J. Gaubicher, S. Renault, L. Dubois, Y. Liang, and Y. Yao. Opportunities and challenges for organic electrodes in electrochemical energy storage. Chemical Reviews, 120(14):6490–6557, 2020.
- [5] H. Yang, J. Lee, J. Y. Cheong, Y. Wang, G. Duan, H. Hou, S. Jiang, and I.-D. Kim. Molecular engineering of carbonyl organic electrodes for rechargeable metal-ion batteries: fundamentals, recent advances, and challenges. Energy & Environmental Science, 14:4228–4267, 2021.
- [6] Z. Huang, X. Du, M. Ma, S. Wang, Y. Xie, Y. Meng, W. You, and L. Xiong. Organic cathode materials for rechargeable aluminum-ion batteries. ChemSusChem, 16(9):637–671, 2023.
- [7] Z. Li, J. Häcker, M. Fichtner, and Z. Zhao-Karger. Cathode materials and chemistries for magnesium batteries: challenges and opportunities. Advanced Energy Materials, 13(27), 2023.
- [8] Y. Chen, K. Fan, Y. Gao, and C. Wang. Challenges and perspectives of organic multivalent metal-ion batteries. Advanced Materials, 34(52):2200662, 2022.
- [9] P. Poizot, F. Dolhem, and J. Gaubicher. Progress in all-organic rechargeable batteries using cationic and anionic configurations: toward low-cost and greener storage solutions? Current Opinion in Electrochemistry, 9:70–80, 2018.

- [10] M. Kolek, F. Otteny, P. Schmidt, C. Mück-Lichtenfeld, C. Einholz, J. Becking, E. Schleicher, M. Winter, P. Bieker, and B. Esser. Ultra-high cycling stability of poly(vinylphenothiazine) as a battery cathode material resulting from  $\pi$ - $\pi$  interactions. Energy & Environmental Science, 10:2334–2341, 2017.
- [11] M. Kolek, F. Otteny, J. Becking, M. Winter, B. Esser, and P. Bieker. Mechanism of charge/discharge of poly(vinylphenothiazine)-based li-organic batteries. Chemistry of Materials, 30(18):6307–6317, 2018.
- [12] F. Otteny, V. Perner, C. Einholz, G. Desmaizieres, E. Schleicher, M. Kolek, P. Bieker, M. Winter, and B. Esser. Bridging the gap between small molecular  $\pi$ -interactions and their effect on phenothiazine-based redox polymers in organic batteries. ACS Applied Energy Materials, 4(8):7622–7631, 2021.
- [13] V. Perner, D. Diddens, F. Otteny, V. Küpers, P. Bieker, B. Esser, M. Winter, and M. Kolek. Insights into the solubility of poly(vinylphenothiazine) in carbonate-based battery electrolytes. ACS Applied Materials & Interfaces, 13(10):12442–12453, 2021.
- [14] B. Tengen, T. Winkelmann, N. Ortlieb, V. Perner, G. Studer, M. Winter, B. Esser, A. Fischer, and P. Bieker. Immobilizing poly(vinylphenothiazine) in ketjenblack-based electrodes to access its full specific capacity as battery electrode material. Advanced Functional Materials, 33(9):2210512, 2023.
- [15] F. Otteny, M. Kolek, J. Becking, M. Winter, P. Bieker, and B. Esser. Unlocking full discharge capacities of poly(vinylphenothiazine) as battery cathode material by decreasing polymer mobility through cross-linking. Advanced Energy Materials, 8(33):1802151, 2018.
- [16] G. Studer, A. Schmidt, J. Büttner, M. Schmidt, A. Fischer, I. Krossing, and B. Esser. On a high-capacity aluminium battery with a two-electron phenothiazine redox polymer as a positive electrode. Energy & Environmental Science, 16:3760–3769, 2023.
- [17] M. Bhosale, C. Schmidt, P. Penert, G. Studer, and B. Esser. Anion-rocking chair batteries with tuneable voltage using viologen- and phenothiazine polymer-based electrodes\*\*. ChemSusChem, 17(5):e202301143, 2024.

- [18] G. Desmaizieres, V. Perner, D. Wassy, M. Kolek, P. Bieker, M. Winter, and B. Esser. Evaluating the polymer backbone – vinylene versus styrene – of anisyl-substituted phenothiazines as battery electrode materials. Batteries & Supercaps, 6(2):e202200464, 2023.
- [19] F. Otteny, G. Studer, M. Kolek, P. Bieker, M. Winter, and B. Esser. Phenothiazine-functionalized poly(norbornene)s as high-rate cathode materials for organic batteries. ChemSusChem, 13(9):2232–2238, 2020.
- [20] P. Acker, L. Rzesny, C.r F. N. Marchiori, C. M. Araujo, and B. Esser.  $\pi$ -conjugation enables ultra-high rate capabilities and cycling stabilities in phenothiazine copolymers as cathode-active battery materials. Advanced Functional Materials, 29(45):1906436, 2019.
- [21] P. Acker, J. S. Wössner, G. Desmaizieres, and B. Esser. Conjugated copolymer design in phenothiazine-based battery materials enables high mass loading electrodes. ACS Sustainable Chemistry & Engineering, 10(10):3236–3244, 2022.
- [22] R. Wessling, R. Delgado Andrés, I. Morhenn, P. Acker, W. Maftuhin, M. Walter, U. Würfel, and B. Esser. Phenothiazine-based donor–acceptor polymers as multifunctional materials for charge storage and solar energy conversion. Macromolecular Rapid Communications, 45(1):2200699, 2024.
- [23] R. Delgado Andrés, R. Wessling, J. Büttner, L. Pap, A. Fischer, B. Esser, and U. Würfel. Organic photo-battery with high operating voltage using a multi-junction organic solar cell and an organic redox-polymer-based battery. Energy & Environmental Science, 16:5255–5264, 2023.
- [24] R. Wessling, H. Koger, F. Otteny, M. Schmidt, A. Semmelmaier, and B. Esser. Unlocking twofold oxidation in phenothiazine polymers for application in symmetric all-organic anionic batteries. ACS Applied Polymer Materials, 6:7956–7968, 2024.
- [25] F. Otteny, G. Desmaizieres, and B. Esser. Phenothiazine-based redox polymers for energy storage. In Redox Polymers for Energy and Nanomedicine, pages 166 – 197. The Royal Society of Chemistry, 2020.

- [26] M. Neumann, M. Ademmer, M. Osenberg, A. Hilger, F. Wilde, S. Muench, M.D. Hager, U.S. Schubert, I. Manke, and V. Schmidt. 3D microstructure characterization of polymer battery electrodes by statistical image analysis based on synchrotron x-ray tomography. Journal of Power Sources, 542, 2022.
- [27] M. Ademmer, P.-H. Su, L. Dodell, J. Asenbauer, M. Osenberg, A. Hilger, I. Chang, J.-K. and Manke, M. Neumann, V. Schmidt, and D. Bresser. Unveiling the impact of crosslinking redox-active polymers on their electrochemical behavior by 3D imaging and statistical microstructure analysis. The Journal of Physical Chemistry C, 127:19366–19377, 2023.
- [28] T. M. M. Heenan, C. Tan, J. Hack, D. J. L. Brett, and R. P. Shearing. Developments in X-ray tomography characterization for electrochemical devices. Materials Today, 31:69–85, 2019.
- [29] F. Tang, Z. Wu, C. Yang, M. Osenberg, A. Hilger, K. Dong, H. Markötter, I. Manke, F. Sun, L. Chen, and G. Cui. Synchrotron X-Ray tomography for rechargeable battery research: fundamentals, setups and applications. Small Methods, 5(9):2100557, 2021.
- [30] L. Holzer and M. Cantoni. Review of FIB-tomography. In I. Utke, S. Moshkalev, and P. Russell, editors, Nanofabrication using Focused Ion and Electron Beams: Principles and Applications, pages 410–435. Oxford University Press, 2012.
- [31] G. Möbus and B. J. Inkson. Nanoscale tomography in materials science. Materials Today, 10:18–25, 2007.
- [32] S. Berg, D. Kutra, T. Kroeger, C. N. Straehle, B. X. Kausler, C. Haubold, M. Schiegg, J. Ales, T. Beier, M. Rudy, K. Eren, J. I. Cervantes, B. Xu, F. Beuttenmueller, A. Wolny, C. Zhang, U. Koethe, F. A. Hamprecht, and A. Kreshuk. ilastik: interactive machine learning for (bio)image analysis. Nature Methods, 16:1226—1232, 2019.
- [33] M. Neumann, E. Machado Charry, K. Zojer, and V. Schmidt. On variability and interdependence of local porosity and local tortuosity in porous materials: a case study for sack paper. Methodology and Computing in Applied Probability, 23:613–627, 2021.

- [34] M. Neumann, P. Gräfensteiner, E. Machado Charry, U. Hirn, A. Hilger, I. Manke, R. Schennach, V. Schmidt, and K. Zojer. R-vine copulas for data-driven quantification of descriptor relationships in porous materials. Advanced Theory and Simulations, 2024:2301261, 2024.
- [35] D. G. Lowe. Distinctive image features from scale-invariant keypoints. International Journal of Computer Vision, 60:91–110, 2004.
- [36] J. Schindelin, I. Arganda-Carreras, E. Frise, V. Kaynig, M. Longair, T. Pietzsch, S. Preibisch, C. Rueden, S. Saalfeld, B. Schmid, J.-Y. Tinevez, D. J. White, V. Hartenstein, K. Eliceiri, P. Tomancak, and A. Cardona. Fiji: an open-source platform for biological-image analysis. Nature Methods, 9:676–682, 2012.
- [37] L. Breiman. Random forests. Machine Learning, 45:5–32, 2001.
- [38] E. Machado Charry, M. Neumann, J. Lahti, R. Schennach, V. Schmidt, and K. Zojer. Pore space extraction and characterization of sack paper using  $\mu$ -CT. Journal of Microscopy, 272:35–46, 2018.
- [39] L. Holzer, P. Marmet, M. Fingerle, A. Wiegmann, M. Neumann, and V. Schmidt. Tortuosity and Microstructure Effects in Porous Media: Classical Theories, Empirical Data and Modern Methods. Springer, 2023.
- [40] S.N. Chiu, D. Stoyan, W.S. Kendall, and J. Mecke. Stochastic Geometry and Its Applications. J. Wiley & Sons, 3rd edition, 2013.
- [41] J. Ohser and K. Schladitz. 3D Images of Materials Structures: Processing and Analysis. Wiley-VCH, 2009.
- [42] M. B. Clennell. Tortuosity: a guide through the maze. Geological Society, London, Special Publications, 122:299–344, 1997.
- [43] B. Ghanbarian, A. G. Hunt, R. P. Ewing, and M. Sahimi. Tortuosity in porous media: a critical review. Soil Science Society of America Journal, 77(5):1461–1477, 2013.

- [44] M. Neumann, O. Stenzel, F. Willot, L. Holzer, and V. Schmidt. Quantifying the influence of microstructure on effective conductivity and permeability: virtual materials testing. International Journal of Solid and Structures, 184:211–220, 2020.
- [45] B. Prifling, M. Röding, P. Townsend, M. Neumann, and V. Schmidt. Large-scale statistical learning for mass transport prediction in porous materials using 90,000 artificially generated microstructures. Frontiers in Materials, 8:786502, 2021.
- [46] K. Thulasiraman and M.N.S. Swamy. Graphs: Theory and Algorithms. J. Wiley & Sons, 1st edition, 1992.
- [47] H. Bozdogan. Model selection and Akaike’s information criterion (AIC): The general theory and its analytical extensions. Psychometrika, 52:345–370, 1987.
- [48] R. B. Nelsen. An Introduction to Copulas. Springer, 2007.
- [49] M. Neumann, S. E. Wetterauer, M. Osenberg, A. Hilger, P. Gräfensteiner, A. Wagner, N. Bohn, J. R. Binder, I. Manke, T. Carraro, and V. Schmidt. A data-driven modeling approach to quantify morphology effects on transport properties in nanostructured NMC particles. International Journal of Solids and Structures, 280:112394, 2023.
- [50] M. M. Siddiqui. Statistical inference for rayleigh distributions. Journal of Research of the National Bureau of Standards, Sec. D, 68(9):1005–1010, 1964.
- [51] L. S. Kremer, A. Hoffmann, T. Danner, S. Hein, B. Prifling, D. Westhoff, C. Dreer, A. Latz, V. Schmidt, and M. Wohlfahrt-Mehrens. Manufacturing process for improved ultra-thick cathodes in high-energy lithium-ion batteries. Energy Technology, 8(2):1900167, 2020.



## Supplementary information

### *Details of image segmentation*

For image segmentation, i.e., for classifying the voxels as pores or solid, the following features are used: Gaussian smoothing, Laplacian of Gaussian, Gaussian gradient magnitude, difference of Gaussians, structure tensor eigenvalues, and Hessian of Gaussian eigenvalues, each one for  $\sigma \in \{0.3, 0.7, 1.0, 1.6, 3.5, 5.0, 10.0\}$ . The output of the trained random forests is a probability map, indicating the probability whether a voxel belongs to the pore space or to the solid phase. Each voxel that belongs to the solid phase with probability greater than 0.4 is assigned to solid phase and otherwise to background, leads to a segmentation into the solid phase and its complement. Note that this threshold has been manually determined based on visual inspection, where we used the open-source software Fiji.

### *Univariate probability density functions*

The probability density functions  $f : \mathbb{R} \rightarrow [0, \infty)$  of the distributions introduced in Section 4.2.1 and used to model the univariate distributions of local morphological descriptors in Section 5.1.1 are provided in the following.

1. Mixture of two Beta distributions  $\mathbf{Beta}(\alpha_1, \alpha_2, \beta_1, \beta_2, p_B)$

$$f(x) = p_B \frac{\Gamma(\alpha_1 + \beta_1) x^{\alpha_1-1} (1-x)^{\beta_1-1}}{\Gamma(\alpha_1) \Gamma(\beta_1)} + (1-p_B) \frac{\Gamma(\alpha_2 + \beta_2) x^{\alpha_2-1} (1-x)^{\beta_2-1}}{\Gamma(\alpha_2) \Gamma(\beta_2)},$$

for each  $x \in [0, 1]$ , where  $\alpha_1, \alpha_2, \beta_1, \beta_2 > 0$  and  $0 \leq p_B \leq 1$ .

2. Mixture of two Gaussian distributions  $\mathbf{N}(\mu_1, \mu_2, \sigma_1, \sigma_2, p_N)$

$$f(x) = p_N \frac{1}{\sigma_1 \sqrt{2\pi}} \exp\left(-\frac{(x - \mu_1)^2}{2\sigma_1^2}\right) + (1-p_N) \frac{1}{\sigma_2 \sqrt{2\pi}} \exp\left(-\frac{(x - \mu_2)^2}{2\sigma_2^2}\right)$$

for each  $x \in \mathbb{R}$ , where  $\mu_1, \mu_2 \in \mathbb{R}$ ,  $\sigma_1, \sigma_2 > 0$  and  $0 < p_N < 1$ .

3. Maxwell-Boltzmann distribution  $\mathbf{MB}(\mu_M, \sigma_M)$

$$f(x) = \sqrt{\frac{2}{\pi}} \frac{(x - \mu_M)^2}{\sigma_M^2} \exp\left(-\frac{(x - \mu_M)^2}{2\sigma_M^2}\right),$$

for each  $x > \mu_M$ , where  $\mu_M \in \mathbb{R}$  and  $\sigma_M > 0$ .

4. Shifted Gamma distribution  $\Gamma(a_\Gamma, \sigma_\Gamma, \mu_\Gamma)$

$$f(x) = \frac{1}{\Gamma(a_\Gamma)} \left( \frac{x - \mu_\Gamma}{\sigma_\Gamma} \right)^{a_\Gamma - 1} \exp \left( -\frac{x - \mu_\Gamma}{\sigma_\Gamma} \right),$$

for each  $x > \mu_\Gamma$ , where  $a_\Gamma, \sigma_\Gamma > 0$  and  $\mu_\Gamma \in \mathbb{R}$ .

5. Rayleigh distribution  $R(\mu_R, \sigma_R)$

$$f(x) = \frac{x - \mu_R}{\sigma_R} \exp \left( -\frac{(x - \mu_R)^2}{2\sigma_R^2} \right),$$

for each  $x > \mu_R$ , where  $\mu_R \in \mathbb{R}$  and  $\sigma_R > 0$ .

### *Brief introduction to copulas*

We briefly recall the concept of copulas. Let  $(U, V)$  be a two-dimensional random vector taking values in the unit square  $[0, 1]^2$ , where  $U$  and  $V$  are uniformly distributed on the unit interval  $[0, 1]$ . Then, the joint probability distribution function  $C : [0, 1]^2 \rightarrow [0, 1]$  of  $(U, V)$  is called a two-dimensional copula, where  $C(u, v) = P(U \leq u, V \leq v)$  with  $P(U \leq u) = u$  and  $P(V \leq v) = v$  for any  $u, v \in [0, 1]$ . From Sklar's representation formula [48] we get that for any two-dimensional random vector  $(X, Y)$ , its joint probability distribution function  $H : \mathbb{R}^2 \rightarrow [0, 1]$  with  $H(x, y) = P(X \leq x, Y \leq y)$  can be written in the form

$$H(x, y) = C(F(x), G(y))$$

for all  $x, y \in \mathbb{R}$ , where  $F : \mathbb{R} \rightarrow [0, 1]$  with  $F(x) = P(X \leq x)$  for each  $x \in \mathbb{R}$  and  $G : \mathbb{R} \rightarrow [0, 1]$  with  $G(y) = P(Y \leq y)$  for each  $y \in \mathbb{R}$  are the univariate distribution functions of  $X$  and  $Y$ , respectively, and  $C : [0, 1]^2 \rightarrow [0, 1]$  is a certain copula. Moreover, if the functions  $F, G$  and  $C$  are differentiable, then the joint probability density  $h : \mathbb{R}^2 \rightarrow [0, \infty)$  of  $(X, Y)$  can be written as

$$h(x, y) = f(x)g(y) \left( \frac{\partial^2}{\partial x \partial y} C \right) (F(x), G(y))$$

for all  $x, y \in \mathbb{R}$ , where  $f : \mathbb{R} \rightarrow [0, \infty)$  and  $g : \mathbb{R} \rightarrow [0, \infty)$  are the univariate probability densities of  $X$  and  $Y$ , respectively. From the joint probability density, we directly obtain the

conditional probability density  $h_{Y=y} : \mathbb{R} \rightarrow [0, \infty)$  of  $X$  given  $Y = y$  for each  $y \in \mathbb{R}$  fulfilling  $g(y) > 0$ . It reads as

$$h_{Y=y}(x) = f(x) \left( \frac{\partial^2}{\partial x \partial y} C \right) (F(x), G(y))$$

for each  $x \in \mathbb{R}$ .